PAPER

Low-temperature densification of Al-doped Li$_7$La$_3$Zr$_2$O$_{12}$: a reliable and controllable synthesis of fast-ion conducting garnets†

Hany El-Shinawi,[a] Gary W. Paterson,[b] Donald A. MacLaren,[b] Edmund J. Cussen*[c] and Serena A. Corr*[a]

The application of Li$_7$La$_3$Zr$_2$O$_{12}$ as a Li$^+$ solid electrolyte is hampered by the lack of a reliable procedure to obtain and densify the fast-ion conducting cubic garnet polymorph. Dense cubic Li$_7$La$_3$Zr$_2$O$_{12}$-type phases are typically formed as a result of Al-incorporation in an unreliable reaction with the alumina crucible at elevated temperatures of up to 1230 °C. High Al^{3+}-incorporation levels are also believed to hinder the three-dimensional movement of Li$^+$ in these materials. Here, a new, facile hybrid sol–gel solid-state approach has been developed in order to accomplish reliable and controllable synthesis of these phases with low Al-incorporation levels. In this procedure, sol–gel processed solid precursors of Li$_7$La$_3$Zr$_2$O$_{12}$ and Al$_2$O$_3$ nanosheets are simply mixed using a pestle and mortar and allowed to react at 1100 °C for 3 h to produce dense cubic phases. Fast-ion conducting Al-doped Li$_7$La$_3$Zr$_2$O$_{12}$ phases with the lowest reported Al^{3+}-content (~0.12 mol per formula unit), total conductivities of ~3 × 10^{-4} S cm^{-1}, bulk conductivities up to 0.6 mS and ion conduction activation energies as low as 0.27 eV, have been successfully achieved. The ease of lithium diffusion in these materials is attributed to the formation of dense cubic phases with low Al^{3+} dopant ratios. This approach is applicable to Li$_{7-x}$La$_3$Zr$_{2-x}$Ta$_x$O$_{12}$ phases and opens up a new synthetic avenue to Li$_7$La$_3$Zr$_2$O$_{12}$-type materials with greater control over resulting characteristics for energy storage applications.

1.   Introduction

Among the lithium stuffed garnets, Li$_7$La$_3$Zr$_2$O$_{12}$ (LLZO)-type phases display the highest bulk and grain boundary Li$^+$ conductivity at room temperature (>1 × 10^{-4} S cm^{-1}), as well as excellent stability in contact with lithium metal and in aqueous solutions.[1,2] LLZO is therefore a promising ceramic component for manufacturing Li$^+$ solid electrolyte membranes, which are expected to play a key role in next-generation lithium battery technologies such as all-solid-state, lithium–sulfur and lithium–air batteries. The ease of Li$^+$ diffusion in lithium stuffed garnets is attributed to the existence of three-dimensional interconnected channels of partially occupied Li$^+$ lattice sites, which supports a cubic symmetry of the garnet structure.[3,4] Fast-ion conducting cubic LLZO-type phase was first reported by Murugan et al. by annealing stoichiometric mixtures of starting materials in alumina crucibles at elevated temperatures

(>1200 °C).[1] Al^{3+} incorporation from the alumina crucible was later found to be responsible for stabilization and densification of the fast-ion conducting phase.[5,6] Unlike heavy metal doping (e.g. with Ta), this "light element" incorporation in LLZO was accompanied by densification of the material. This study was followed by numerous attempts to synthesize Al-doped LLZO phases using more reliable and commercially desirable procedures. The aim was to reduce reaction times, to eliminate repeated homogenization steps such as ball milling, and to avoid reactions with the crucible by reducing the reaction temperature. Decreases in reaction temperatures are of particular interest if these materials are to find industrial uptake, for example in the future development of all solid-state batteries. Attempts included syntheses by solid-state reactions using Al additives[6–8] or syntheses using solution-based methods with or without Al additives.[9–12] Other light elements, such as Ga, have also been successfully investigated as stabilisers for the cubic garnet phase.[13] The successful preparation of fast-ion conducting phases, however, often requires the use of elevated temperatures (≥1200 °C) and, in several cases, the use of alumina crucibles which provide a source of additional dopant. Al-Doped phases produced at lower calcination temperatures (700–1100 °C) typically lack phase purity and/or sufficient Li$^+$ conductivity,[14,15] and often require elaborate densification procedures.[11,16,17] The difficulty in developing an alternative

^{a}School of Chemistry, University of Glasgow, Glasgow G12 8QQ, UK. E-mail: serena.corr@glasgow.ac.uk

^{b}School of Physics and Astronomy, University of Glasgow, Glasgow G12 8QQ, UK

^{c}WestCHEM, Department of Pure and Applied Chemistry, The University of Strathclyde, Thomas Graham Building, 295 Cathedral Street, Glasgow, G1 1XL, UK

† Electronic supplementary information (ESI) available. See DOI: 10.1039/c6ta06961d

This journal is © The Royal Society of Chemistry 2017

J. Mater. Chem. A, 2017, 5, 319–329 | 319

approach to produce fast-ion conducting Al-doped LLZO phases arises from the fact that the formation and the densification of the material are correlated. The desired cubic polymorph is likely formed during the densification process where Al plays the key role in this process. Al^{3+} incorporates in the garnet lattice creating vacancies and thereby stabilizing the cubic phase.[5,6] In the presence of excess lithium and at sufficient sintering temperatures, Al-incorporation also helps to densify the material and thereby preserves the structural integrity by suppressing lithium depletion from the compound.

Much effort has been undertaken to determine the site preference of Al^{3+}, and similar dopants such as Ga^{3+}, in the cubic LLZO.[5,6,18–25,27] Al magic angle spinning (MAS) nuclear magnetic resonance (NMR) spectra of Al-doped LLZO showed two characteristic resonances at *ca.* 66 ppm and *ca.* 80 ppm. The resonance near 66 ppm is consistently assigned to Al^{3+} located at the 24d sites in cubic LLZO,[5,6,18–21] while the resonance at approximately 80 ppm has been assigned to the 96h position according to density functional theory (DFT) studies.[20,21] DFT calculations, however, also indicate that the 24d site is energetically favorable for Al^{3+} over the 96h position;[22] moreover, they give evidence that Al^{3+} could occupy the octahedral 48g sites.[20] Neutron powder diffraction (NPD) studies, on the other hand, have located Al^{3+} at the 24d sites[6,13,14,23] or, in one report, at the 48g sites.[24] The site preference of Al^{3+} is expected to have a significant influence on the transport properties of LLZO since the 24d sites joint the loops of the Li^+ pathways in LLZO.[22,23] The site preference of Al^{3+} in the 24d sites would therefore hinder the three-dimensional movement of Li^+.[22,23] Hence, in addition to the need for an alternative synthesis of Al-doped LLZO, the preparation of lightly-doped phases, which preserve the required sinterability, is also favoured. Here, we aimed to accomplish a low-temperature densification of Al-doped LLZO in order to achieve both reliable synthesis and low Al^{3+}-incorporation levels.

2. Experimental section

2.1 Synthesis

Sol–gel synthesis of LLZO. Lithium acetate (99.95%, Aldrich), lanthanum oxide (≥99.9%, Aldrich) and zirconium oxynitrate hydrate (99%, Aldrich) were used as starting materials. The formula weight of zirconium oxynitrate was determined thermogravimetrically, and lanthanum oxide was dried at 900 °C for 12 h prior to use. Stoichiometric amounts of the starting materials according to Li/La/Zr molar ratio of 7.7 : 3 : 2.1 were dissolved in a mixture of acetic acid/water (80 : 20, volume ratio) at ∼80 °C (solution A). Equal volume of ammonium hydroxide solution (28.0–30.0% NH_3, Aldrich) is used to dissolve an equivalent amount of EDTA (metal ions to EDTA molar ratio is 1 : 1.5) (solution B). Solution B is carefully added to solution A, and the mixture was evaporated at 120 °C without further adjustment of the pH. The brown gel obtained is then burnt out at 550–600 °C, until a white solid precursor is obtained. This white precursor is pre-calcined at 900 °C for 1 h, to initiate the formation of the garnet phase.

Sol–gel synthesis of amorphous aluminium oxide. An appropriate amount of aluminium acetylacetonate (99%, Aldrich) was dissolved in acetic acid/water mixture according to the previous sol–gel procedure. The obtained white solid precursor in this case was preheated at 750 °C for 2 h.

Formation of the Al-doped LLZO. Stoichiometric amounts of the LLZO solid precursor and the aluminium oxide precursor were mixed using a pestle and mortar in order to produce LLZO phases doped with ∼2 wt% Al. Typically, 1 g of the LLZO solid precursor is mixed with 0.04 g of the aluminium oxide precursor. This mixture was pressed uniaxially to form pellets, which are placed into a thick platinum sheet and heated to 1000 or 1100 °C for 3 h using a microwave hybrid furnace (CEM Phoenix). To minimize the contact between the platinum sheet and the LLZO pellet, the pellet was placed on top of another thin pellet of the same composition. The surface of the pellet was not covered with the mother powder. The produced pellets were either used as-prepared (or after polishing) for impedance measurements or crushed for other analyses. Freshly prepared pellets were used in all analyses; otherwise, pellets were stored in a glovebox under argon to avoid any possible Li^+/H^+ exchange.

Conventional sol–gel synthesis of Al-doped LLZO. The starting materials including aluminium acetylacetonate were dissolved in acetic acid/water mixture per the previous sol–gel procedure. After drying the gel and obtaining the white solid precursor, the powder was pressed into pellets and calcined at 1100 °C, for 3 h using a microwave hybrid furnace.

2.2 Characterization methods

X-ray diffraction (XRD) studies were performed using a PANalytical X'Pert PRO diffractometer in reflection mode using Cu-Kα radiation. Neutron powder diffraction (NPD) data were collected using the Polaris instrument at the ISIS facility, Rutherford Appleton Laboratory, UK. A multi-histogram Rietveld fit to Polaris detector banks 4 and 5 was done using the GSAS and EXPGUI suite of programmes.[26] Induced coupled plasma-mass spectroscopy (ICP-MS) analysis was performed using an Agilent 7700 ICP-MS instrument. Scanning electron microscopy (SEM) studies were performed using Carl Zeiss Sigma variable pressure analytical electron microscope. In addition to secondary electron detectors, the machine is equipped with an angle selective backscattered electron detector (AsB), to obtain a materials contrast image. Transmission electron microscopy (TEM) was performed on a JEOL ARM 200cF microscope equipped with a cold field emission gun and operated at 200 kV. Electron energy-loss spectroscopy (EELS) spectra were taken with a Gatan 965 Quantum ER spectrometer and the energy-dispersive X-ray spectroscopy (EDS) data were taken with a Bruker XFlash (60 mm^2) EDS detector. Gas sorption measurements were performed using a Quantachrome Quadrasorb Evo gas sorption analyser using nitrogen as the adsorbate gas.

AC impedance measurements were recorded using a Solartron 1260 impedance analyzer in the frequency range of 3 MHz to 1 Hz (an electrical perturbation of 50 mV) using gold

320 | *J. Mater. Chem. A*, 2017, **5**, 319–329

This journal is © The Royal Society of Chemistry 2017

electrodes. Gold electrodes were gas-phase deposited on the circular sides of the pellets by thermal evaporation and platinum wires were used to collect the current. Variable temperature conductivity measurements were carried out in the temperature range 25–120 °C. Prior to each impedance measurement, the samples were equilibrated for 30 min at constant temperature.

3. Results and discussion

We have studied the stabilization and densification of fast-ion conducting LLZO phases in the presence of amorphous alumina nanosheets (developed in this study for this purpose) in the temperature range of 1000 to 1100 °C. Fig. 1 shows a schematic representation of typical LLZO-densification by interaction with the alumina crucible at elevated temperatures, together with our proposed lower temperature approach. The conditions depicted in Fig. 1b which avoid prolonged calcination at elevated temperatures are commercially desirable and favour interfacial reactions between LLZO and the Al-precursor. We found that if the garnet phase (depicted in green in Fig. 1) contains an excess of Li and Zr, a mixture of $LiAlO_2/Li_2ZrO_3$ is formed *in situ* which helps to stabilize and densify the cubic phase at relatively low calcination temperatures. A schematic representation of the hybrid sol–gel solid-state synthesis employed, along with the conventional sol–gel synthesis, is displayed in Fig. 2.

The synthesized Al_2O_3 solid precursor has been characterized by XRD, SEM, TEM and selected area electron diffraction (SAED) techniques (Fig. 3). The XRD pattern of the material (Fig. 3a) shows undefined broad peaks, suggesting that the material is amorphous. SEM images (Fig. 3b) reveal a morphology composed of non-uniform nanosheets, approximately 50 to 100 nm thick and several tens of micrometres wide. The microstructure and crystallinity of the material were further examined by TEM and SAED. TEM indicates that the thickness of the sheets varies significantly between particles, while each

particle has a uniform thickness. From scanning transmission electron microscopy and electron energy-loss spectroscopy (STEM-EELS) measurements on several particles, and using typical values for the density of the Al_2O_3, the material thickness is in the range of 40 to 140 nm. Fig. 3c shows low magnification TEM, high resolution TEM (HRTEM), and SAED images of the same area of one particle. The HRTEM image shows that the material is highly disordered with a degree of polycrystallinity indicated by the diffuse diffraction rings in the SAED pattern. The rings identified in the diffraction pattern are consistent with a lower oxygen content cubic alumina phase (Al_2O_{3-x}),[27] possibly induced by the electron beam. Finally, the specific surface area of the material is determined from nitrogen adsorption using the Brunauer–Emmett–Teller (BET) method. The material showed a relatively large specific surface area of 59.4 m^2 g^{-1}.

The LLZO precursor (initially containing 10 mol% excess of Li and 5 mol% excess of Zr) was mixed with stoichiometric amounts of the Al_2O_3 precursor in order to achieve $Li_7La_3Zr_2O_{12}$ phases containing 2 wt% Al (~0.6 mol per formula unit). The mixtures were calcined at either 1000 °C or 1100 °C for 3 h. ICP-MS analysis of one sample after calcination at 1100 °C reveals an Al content of 1.95(1) wt% which indicates that the Al content is accurately controlled by the experimental procedure. Fig. 4 shows the XRD patterns of the calcined materials. The cubic LLZO phase is clearly stabilized at the two calcination temperatures (1000 °C and 1100 °C). Fig. 4 also reveals the formation of minor secondary phases of $LiAlO_2$ and Li_2ZrO_3. The formation of these phases is consistent with using an excess of Li, Al and Zr during the synthesis process. These excesses were selected carefully to optimize the purity and crystallinity of the cubic LLZO phase, as revealed by XRD analyses. Using lower concentrations of Al or Zr led to the disappearance of the impurity phases, but, undesirably, resulted in significant peak broadening and splitting in the XRD patterns suggesting inadequate stabilization of the cubic phase (Fig. S1–S3†).
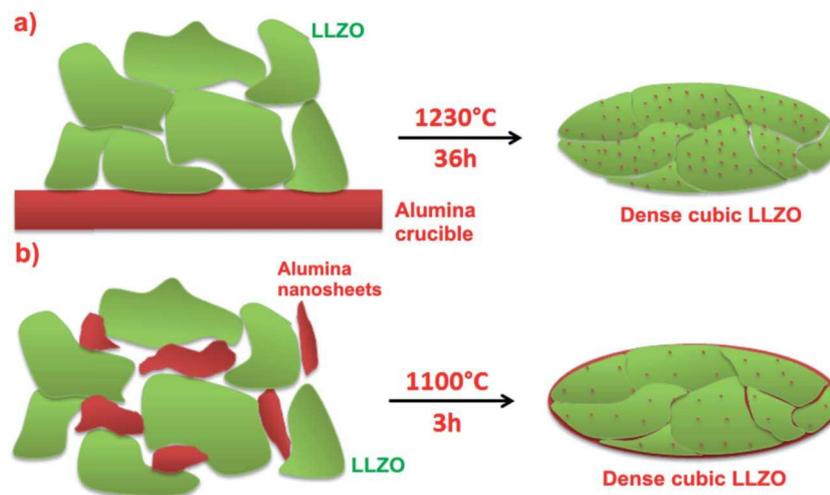

Fig. 1 A schematic representation of stabilization and densification of fast-ion conducting LLZO by (a) interaction with the alumina crucible at 1230 °C, and (b) our proposed interaction with nanostructured alumina at 1100 °C.
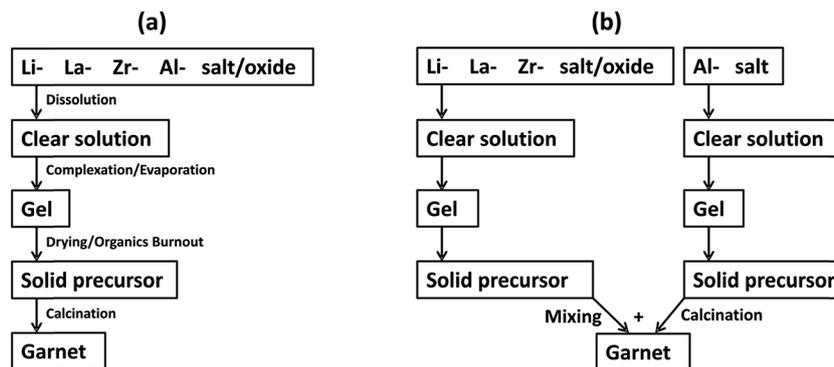
Fig. 2 A schematic representation of (a) a conventional sol–gel procedure, and (b) our proposed hybrid sol–gel solid-state procedure for obtaining fast-ion conducting garnet phases.
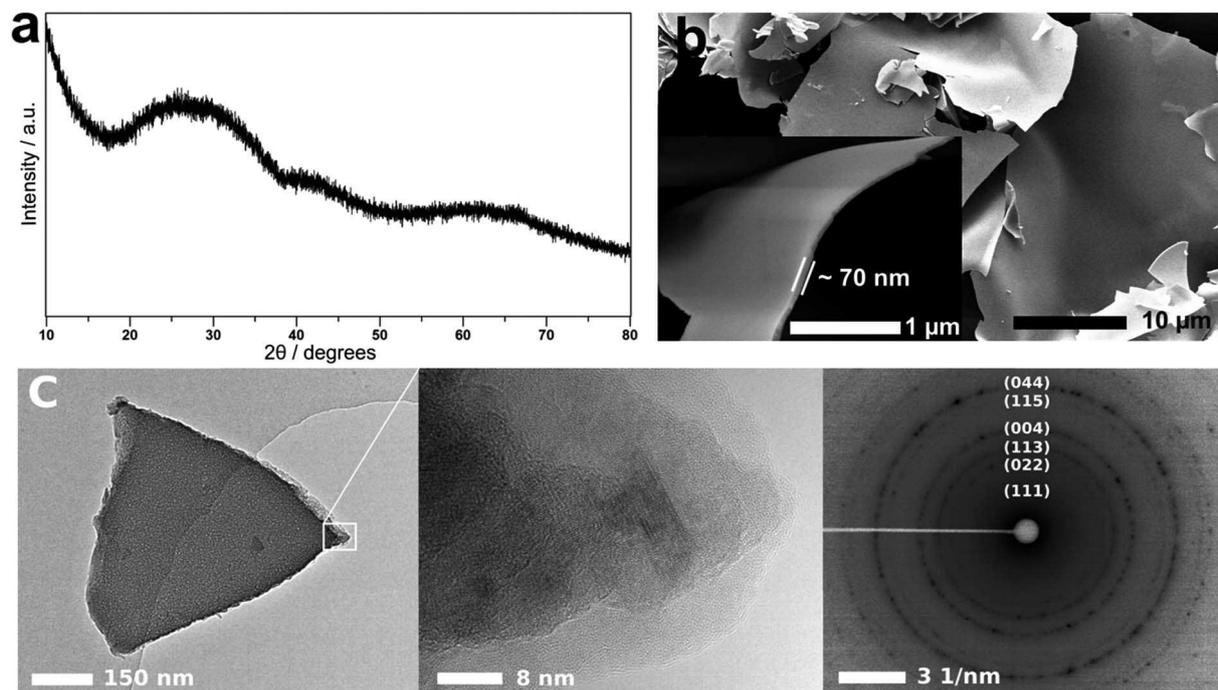

Fig. 3 XRPD pattern (a), SEM image (b), and HRTEM/SAED analysis (c) of the Al_2O_3 solid precursor.

A room temperature NPD pattern was collected for the sample calcined at 1100 °C and a Rietveld structure refinement was performed using the GSAS suite of programs. The secondary phases $LiAlO_2$ and Li_2ZrO_3 were detected in the neutron diffraction pattern; no La-containing impurities (*e.g.* $LaAlO_3$) were detected. The impurity phases were introduced in the structure refinement. The refined unit cell parameter a is 12.9713(2) Å, in good agreement with the LLZO phase made by conventional solid-state reaction at 1230 °C ($a = 12.9682(6)$ Å).[1] The refinement was performed with the garnet framework atoms La, Zr, and O located at 24c, 16a and 96h sites, respectively, and lithium located at the 24d and 96h sites. The Al content was fixed[6,15,23] to the value revealed from EDS analysis (0.12 mol per formula unit; see below) and placed into the tetrahedral 24d sites.[6,13,15,23] Attempts to distribute Al between the 24d and 96h sites in accordance with NMR studies[20,21] were unsuccessful, yielding negative occupation of the 96h sites. A significant improvement of the refinement was observed by refining the occupancy of the Zr-site, leading to a slight Zr deficiency in the compound. The lithium content was finally constrained to a value which agrees with charge neutrality. The refinement revealed a $LiAlO_2$ secondary phase with a weight fraction corresponding to 0.48(8) mol per formula unit. The sum of the Al content in the material is therefore ~0.6 mol per formula unit, in good agreement with the experimental procedure. The refinement hence confirms the EDS results and suggests the incorporation of ~0.12 mol Al (per formula unit) in the garnet lattice. The refined phase fraction of Li_2ZrO_3 reveals the existence of 0.20(9) mol Li_2ZrO_3 per formula unit. This is consistent with using 5 mol% excess of Zr and the release of
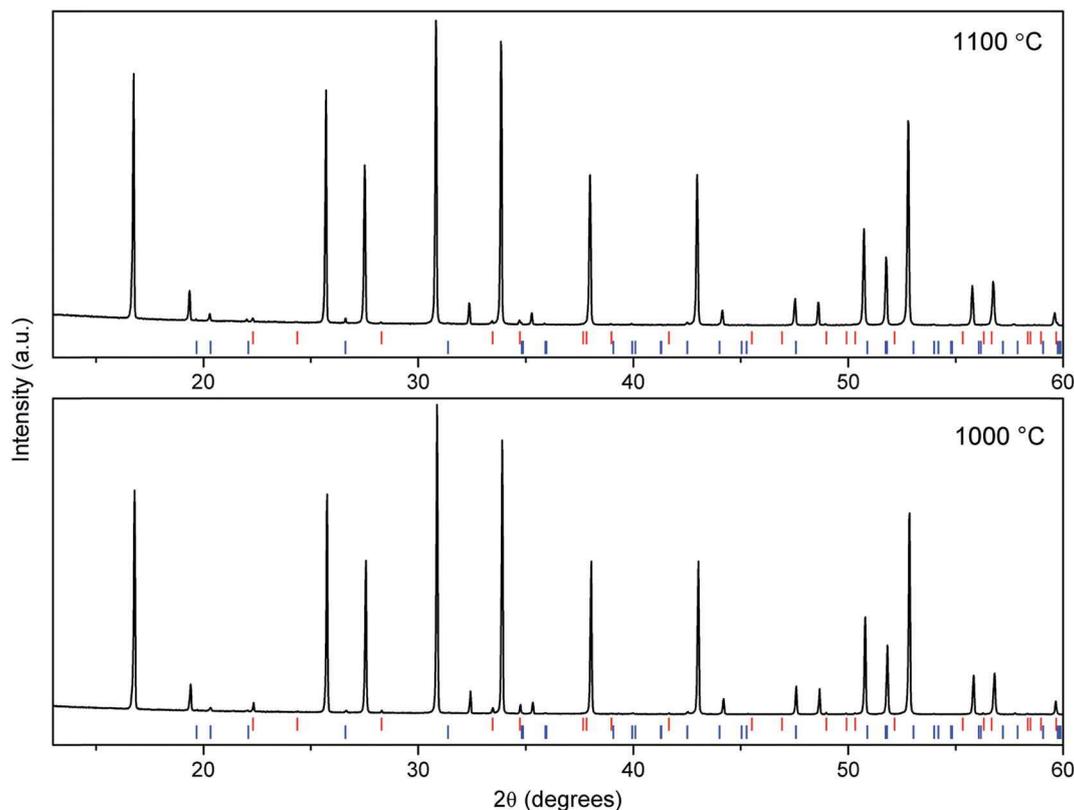
Fig. 4 XRPD patterns for LLZO (2 wt% Al) synthesized by hybrid sol–gel solid-state approach and calcined at 1000 and 1100 °C. The top markers (red) are for $LiAlO_2$ and the bottom markers (blue) are for Li_2ZrO_3.

more Zr on sintering due to the formation of vacancies in the Zr sites. The latter effect is indeed observed by XRD (Fig. 4 and S4†) where the intensities of the Li_2ZrO_3 diffraction peaks increase when a calcination temperature of 1100 °C is employed. The intensities of the $LiAlO_2$ diffraction peaks are decreased when the calcination temperature is increased (Fig. S4†), most likely due to the insertion of Al^{3+} in the lattice. Düvel *et al.* suggested that Zr^{4+} can be replaced by Al^{3+} in heavily doped LLZO phases.[18] Our study gives evidence, however, for a low concentration of vacancies, but not for the existence of Al^{3+} in the Zr sites. The fitted NPD patterns are shown in Fig. 5 and the refined structural parameters are summarized in Table 1.

In addition to preserving the desired cubic phase, the pellets synthesized at 1100 °C were more effectively densified than those calcined at 1000 °C. A single calcination step for 3 h at 1100 °C was therefore sufficient to produce dense cubic LLZO phases. The microstructure of the pellets was examined by SEM and EDS. SEM examination of the surface of the pellets using an angle selective backscattered (AsB) electron detector indicated the formation of a secondary glassy phase on the surface (Fig. S5†). This phase is more prominent in the pellet calcined at 1100 °C. To examine this surface layer, a longitudinal section of the pellet sintered at 1100 °C was examined by SEM and EDS (Fig. 6).

The SEM image and EDS elemental map in Fig. 6a and b clearly distinguish between an Al-rich phase (dark grey or red)

and the LLZO phase (light grey or green). This Al-rich phase accumulates at the surface, with a concentration gradient near the surface. It was possible to remove this surface layer by polishing the surface of the pellet with fine sand paper. Fig. 6c shows the EDS map collected from the surface after polishing, which indicates that the surface layer is effectively removed. This polished surface also shows an appreciable existence of the Al-rich phase between the LLZO grains. Examination of the bulk of the pellet, however, indicates limited and homogenous existence of the Al-rich phase. SEM images and EDS elemental maps of the bulk of the pellet are shown in Fig. 6d–f. Since XRPD and NPD analyses suggest the formation of $LiAlO_2$ and Li_2ZrO_3 as secondary crystalline phases in our material, this Al-rich phase is clearly $LiAlO_2$. The Li_2ZrO_3 phase could indeed be identified as small particles in intimate contact with the LLZO particles (see the arrow in Fig. 6f and S6†). These results are confirmed by XRD analysis of the pellet surface before and after polishing (Fig. 7a).

The XRD pattern collected from the pellet surface before polishing clearly shows intense $LiAlO_2$ diffraction peaks, which almost disappear after polishing. The Li_2ZrO_3 diffraction peaks have also been reduced in intensity after polishing the surface. Traces of $LaAlO_3$ were also observed on the surface; however, these traces did not appear in the XRPD pattern of the material and completely disappear after polishing, which indicate that these traces are formed as a result of a slight decomposition of
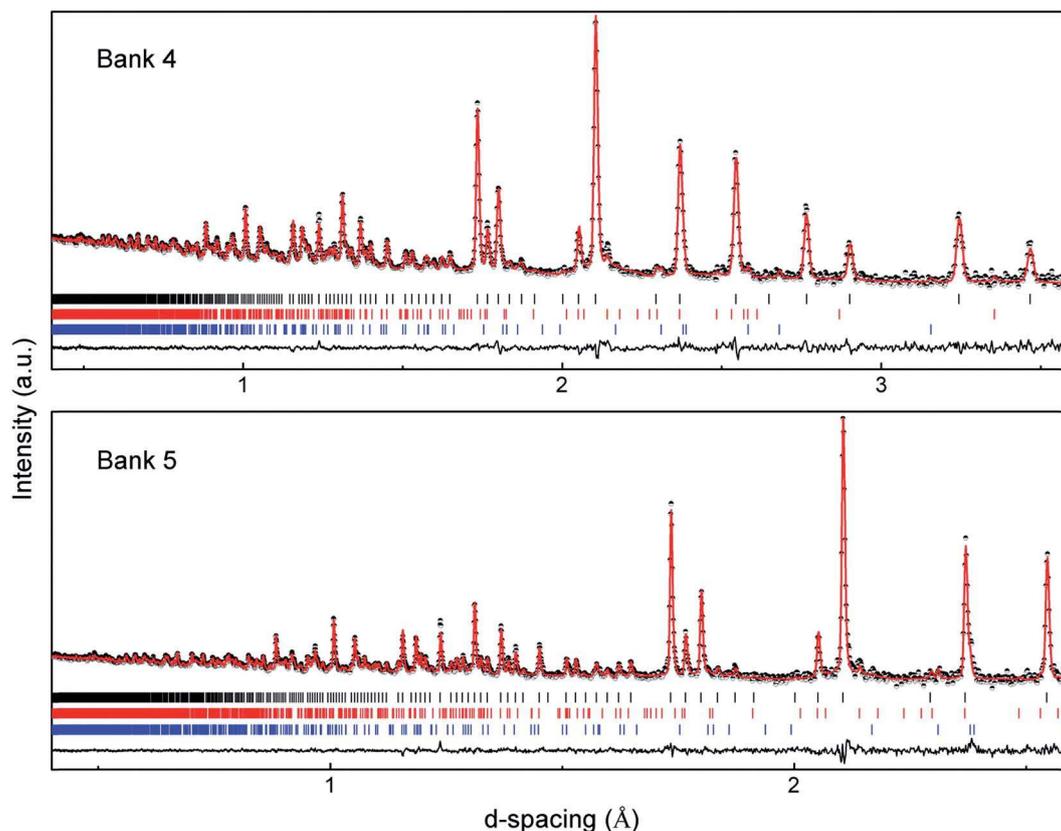
Fig. 5 Rietveld fits to Polaris neutron diffraction data for LLZO (2 wt% Al) calcined at 1100 °C. The top markers (black) are for LLZO; the middle markers (red) are for Li_2ZrO_3; the bottom markers (blue) are for $LiAlO_2$.

Table 1 Refined structural parameters for LLZO (2 wt% Al) calcined at 1100 °C, from Rietveld fits against Polaris neutron powder diffraction data[a]

Atom	Site	Occupation	x	y	z	U_{iso} (Å^2)
Li1	24d	0.444(24)	0.375	0	0.25	0.019(4)
Al	24d	0.04	0.375	0	0.25	0.019(4)
Li2	96h	0.459(6)	0.6905(8)	0.5807(7)	0.0984(7)	0.024(2)
La	24c	1	0.125	0	0.25	0.0075(2)
Zr	16a	0.982(8)	0	0	0	0.0067(4)
O	96h	1	0.28169(9)	0.10003(9)	0.19522(9)	0.0113(3)

[a] Space group $Ia\bar{3}d$, $a = 12.9713(2)$ Å; final fit statistics: $\chi^2 = 1.52$; bank 5: w$R_p = 0.0181$, $R_p = 0.0289$; bank 4: w$R_p = 0.0162$, $R_p = 0.0262$. The sample contains $LiAlO_2$ (3.5(3) wt%) and Li_2ZrO_3 (3.4(3) wt%) secondary phases.

the LLZO phase in the presence of an Al-rich environment at the surface. TEM-EDS analysis of the LLZO particles (Fig. 7b) indicated that the Al-content in the garnet is 0.12(1) mol per formula unit, which is consistent with the refinement results of the NPD data.

The Li$^+$ transport properties of the synthesized materials were studied by impedance spectroscopy using gold blocking electrodes in the temperature range of 25 to 120 °C. Spectra were recorded from the pellets calcined at 1000 and 1100 °C in

order to understand the impedance of this system. Fig. 8a displays a typical Nyquist impedance plot for the pellet calcined at 1000 °C. The plot is characterized by an incomplete high-frequency semicircle, intermediate-frequency semicircle and a low-frequency spike. The impedance data were successfully fitted using a conventional equivalent circuit that employs a constant phase element (CPE) in parallel to a resistance element (R) to represent a semicircle ($[RQ]$), and a constant phase element (CPE) to represent the low frequency spike ($[Q]$) (Fig. 8a).[1,6,28] The capacitance (C) calculated from the fit parameter (Q) and n ($C = (R^{1-n}Q)^{1/n}$) of the high-frequency and intermediate-frequency semicircles are $\sim 6 \times 10^{-11}$ and $\sim 1 \times 10^{-8}$ F, respectively. The latter value for the intermediate-frequency semicircle is too high to account for conventional grain-boundary contributions in this system and, indeed, is characteristic of a surface layer effect.[29,30] Recalling the surface microstructure of this material (Fig. S4†), the surface is partially covered with $LiAlO_2$. The high-frequency semicircle suggests a resistance of ~ 2600 Ω, has an intercept with the high-frequency side of the real Z axis at ~ 1150 Ω, and has a refined capacitance ($\sim 6 \times 10^{-11}$ F) which lies in the range of grain-boundary contributions.[29] This semicircle can be therefore assigned to the "LLZO" grain-boundary contribution. These results suggest a bulk resistance of about one-half of the grain-boundary resistance, which is consistent with the comparatively lower sinterability of the material. This interpretation is
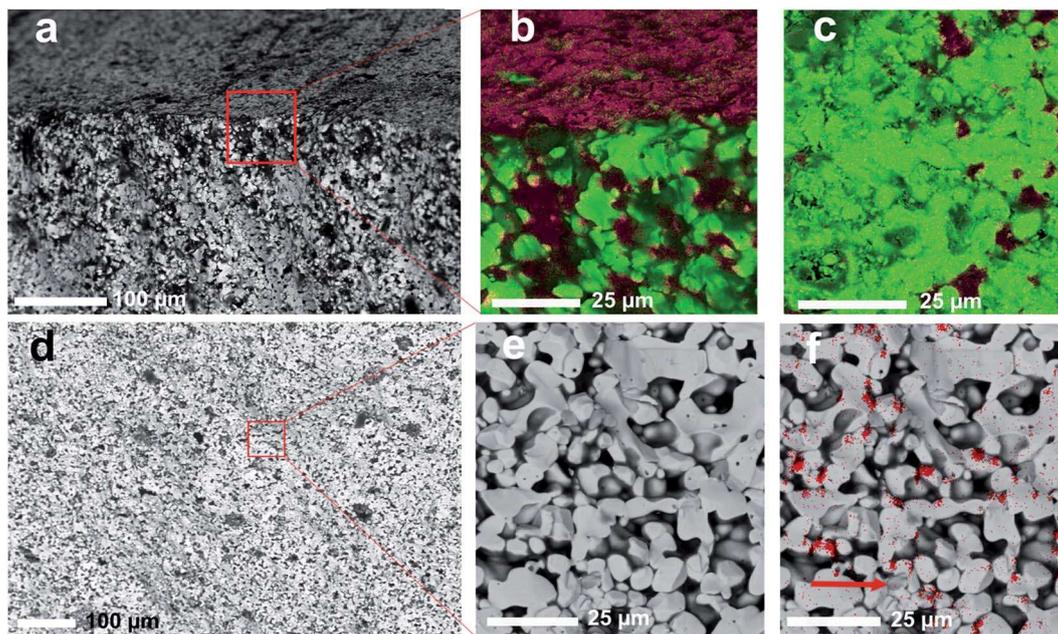
324 | *J. Mater. Chem. A*, 2017, **5**, 319–329

This journal is © The Royal Society of Chemistry 2017

Fig. 6 (a) SEM image of a longitudinal section of the as-prepared LLZO pellet, collected using AsB detector. (b) EDS elemental map of a longitudinal section of the pellet showing the distribution of Zr/La (green) and Al (red). (c) EDS elemental map of the surface of the pellet after polishing (Zr/La (green); Al (red)). (d) and (e) SEM images of the bulk of the pellet collected using AsB detector. (f) EDS elemental map of the bulk of the pellet showing Al distribution (red), the arrow points to a Li_2ZrO_3 particle.

supported by the behaviour of the impedance at higher temperatures (Fig. S7†). As the temperature is increased from room temperature to 120 °C, the high-frequency semicircle disappears while the intermediate-frequency semicircle persists. The former behaviour is consistent with grain-boundary (and bulk) impedance contributions in this type of material,[28] while the latter behaviour is expected for a surface layer. Now we consider the impedance of the pellets calcined at 1100 °C, where the material is well-densified and the effect of the surface layer is expected to be more pronounced. Here, we examine both the as-synthesized and polished pellets in order to carefully study the effect of the Al-rich surface layer on the impedance.

Fig. 8b shows typical Nyquist impedance plots for a pellet before and after polishing. A strong increase of the impedance toward low frequencies is clearly observed for the as-synthesized pellet. The plots, particularly that of the unpolished pellet, are characterized by a poorly-resolved feature in the low frequency range consisting of a broad semicircle and a spike (Fig. 9). In the high-frequency region, the two plots display an incomplete semicircle. Additionally, the impedance of the polished pellet shows an intermediate frequency semicircle (Fig. 9a). Attempts to fit these data using conventional $[RQ]$ and $[Q]$ equivalent circuit elements were unsuccessful. The spectra were, however, fitted using the equivalent circuits $R[RQ][Q[RQ]]$ (unpolished pellet) or $R[RQ][RQ][Q[RQ]]$ (polished pellet) which imply more complex nature of the electrode/surface contributions. Interpretation of the latter contributions is complex, owing to the multiple phases present at the surface, and is beyond the scope of this work.

The impedance plot of the polished pellet is hence similar to the impedance plot observed for the unpolished pellet calcined at 1000 °C. Recalling the microstructure of the polished pellet (Fig. 6c and f) we observe that, although the surface layer is effectively removed, the surface still displays small domains of the Al-rich phase and the bulk has thin films between the grains. This morphology is indeed similar to that of the pellet calcined at 1000 °C, and hence the two samples show similar impedance behaviour. The intermediate frequency semicircle is therefore assigned to surface (interfacial) effects and the high-frequency semicircle is attributed to the "LLZO" grain-boundary contribution. The refined capacitance of the intermediate-frequency semicircle is $\sim 3 \times 10^{-8}$ F which is consistent with a surface layer contribution.[29,30] On the other hand, the surface of the unpolished pellet is covered with a thick layer of $LiAlO_2$ (see Fig. 6a); this magnifies the contribution of the interfacial effects to the impedance, producing the complex feature observed at intermediate and low frequencies in Fig. 9b. In the high-frequency range, the observed semicircle ($C \sim 6 \times 10^{-11}$ F), which nearly coincides with that observed for the polished pellet (taking in account the difference in the pellet dimensions after polishing), is attributed to the "LLZO" grain-boundary resistance. The presence of two different grain-boundary effects, due to the LLZO grains and the interfacial $LiAlO_2$ phase, in these materials is supported by SEM and EDS results.

The plots in Fig. 9 suggest approximately equal bulk and grain-boundary resistances, which is consistent with improving the densification of the material by increasing the calcination temperature. Our results suggest a room temperature (25 °C) total conductivity of $\sim 3 \times 10^{-4}$ S cm^{-1}, and bulk conductivities

This journal is © The Royal Society of Chemistry 2017

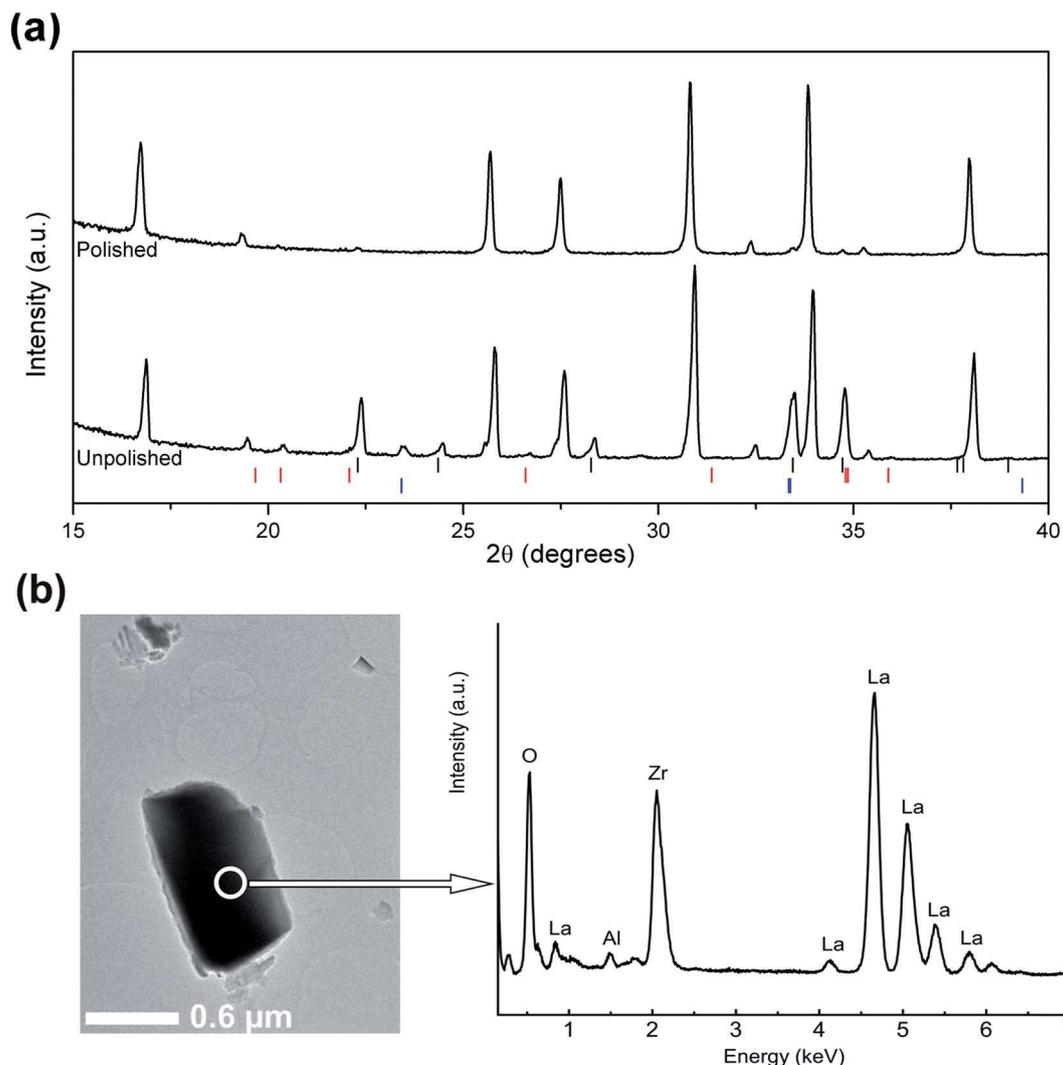J. Mater. Chem. A, 2017, 5, 319–329 | 325

Fig. 7 (a) XRPD patterns collected from the surface of the LLZO pellet before and after polishing. The top markers (black) are for $LiAlO_2$; the middle markers (red) are for Li_2ZrO_3; the bottom markers (blue) are for $LaAlO_3$. (b) TEM-EDS analysis of the LLZO particles; the presented EDS plot is the sum over 6 different particles.

up to 0.6 mS. If the interfacial resistance of the pellet is considered, the material still shows a total conductivity of over 1×10^{-4} S cm^{-1}, which is sufficient for use as a Li$^+$ solid-electrolyte. This is an important achievement considering the advantageous synthesis of the material *via* a 3 h calcination step at 1100 °C.

Impedance spectra were recorded in the temperature range 25–120 °C in order to determine the activation energy for the Li$^+$ transport in these garnets (Fig. S8 and S9†). Similar to the sample calcined at 1000 °C, as the temperature is increased the high-frequency semicircles representing LLZO grain-boundary contributions have disappeared, while the intermediate-frequency semicircle, representing interfacial effects, persisted. The variable temperature studies revealed activation energies of 0.271(5) and 0.285(9) eV for the as-synthesized and polished pellets, respectively. These relatively low activation energies, compared to the reported values for the same material (0.32–0.40 eV),[1,6,11,16,17] suggest a facile Li$^+$ transport in these materials.

We attribute this to the excellent sinterability of the material and the stabilization of the cubic LLZO phase with a low Al^{3+} content.

In order to evaluate our hybrid sol–gel solid-state approach, we have prepared LLZO doped with 2 wt% Al by a conventional sol–gel procedure described in Fig. 2a. The material was characterized by XRD, SEM and impedance spectroscopy. The XRD pattern of the material calcined at 1100 °C (Fig. 10a) reveals the formation of cubic LLZO and minor impurity phases of $LaAlO_3$, $LiAlO_2$ and Li_2ZrO_3. However, in this case the $LaAlO_3$ impurity predominates over $LiAlO_2$, indicating a partial decomposition of the garnet phase. SEM images collected from the pellet (*e.g.* Fig. 10b) indicate that the material is not sufficiently sintered. An Al-rich phase also appears between the grains, however, it lacks the spatial distribution observed in Fig. 6a. A typical Nyquist impedance plot collected from this material at room temperature is shown in Fig. 10c and indicates a total conductivity of $\sim 1.5 \times 10^{-5}$ S cm^{-1}. These results are consistent with
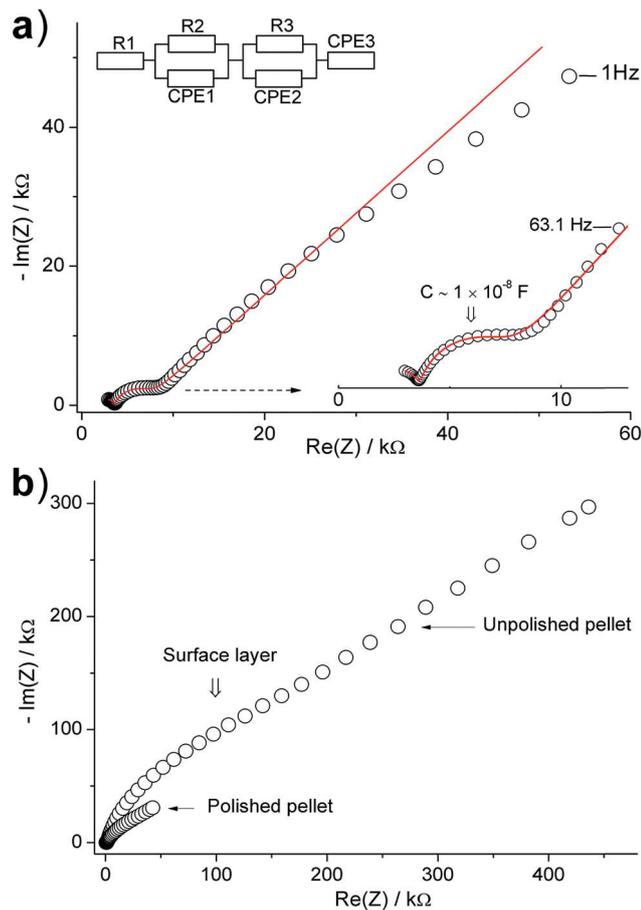
Fig. 8 (a) A typical impedance plot of LLZO (2 wt% Al) calcined at 1000 °C using gold electrodes at room temperature; data were fitted using the presented equivalent circuit $R[RQ][RQ][Q]$. (b) Typical impedance plots of LLZO (2 wt% Al) calcined at 1100 °C before and after polishing (at room temperature).
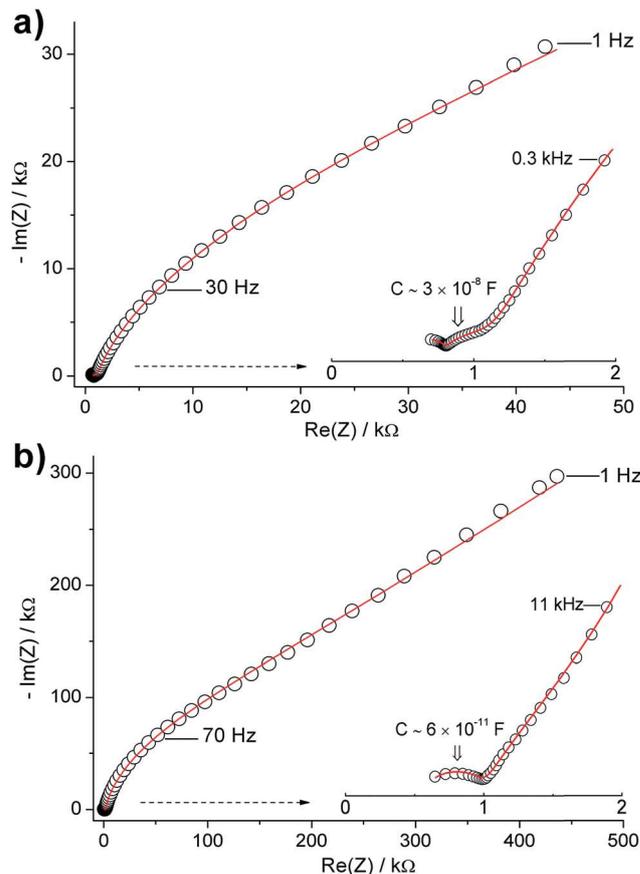

Fig. 9 (a) Typical impedance plot of the polished pellet fitted using the equivalent circuit $R[RQ][RQ][Q[RQ]]$. (b) Typical impedance plot of the unpolished pellet fitted using the equivalent circuit $R[RQ][Q[RQ]]$.

previous studies in which Al-doped LLZO is prepared and densified by conventional sol–gel approaches at temperatures below 1200 °C.[14]

Hence, the newly developed hybrid sol–gel solid-state procedure affords fast-ion conducting LLZO phases, with enhanced sinterability of the cubic LLZO phase compared to conventional sol–gel synthesis, as well as a reliable synthesis at reduced calcination times and temperatures compared to conventional solid-state reactions. Conventional sol–gel syntheses have so far proved unsuccessful to produce fast ion conducting ($\sigma > 1 \times 10^{-4}$ S cm^{-1}) Al-doped LLZO phases at calcination temperatures below 1200 °C. Our study indicates that using excess Al in a conventional sol–gel synthesis also fails to densify the material and leads to the formation of an appreciable LaAlO$_3$ impurity during the calcination step. In the present study, we have used a simple sol–gel procedure to make solid precursors of LLZO and Al$_2$O$_3$ nanosheets which then react at milder, more industrially applicable, conditions (3 h at 1100 °C) to produce fast ion conducting ceramics. This procedure supports (1) homogenous mixing of LLZO components, (2) initiation of the garnet phase formation *via* preheating steps,

and (3) suitable mixing of LLZO and Al precursors that allows appreciable Al^{3+}-incorporation in the lattice and also promotes the interfacial reaction with excess lithium to form LiAlO$_2$ with no appreciable formation of LaAlO$_3$ impurities. The large surface area and amorphous nature of the Al precursor we employ clearly supports the latter function. In the presence of excess Zr, in the form of Li$_2$ZrO$_3$, and LiAlO$_2$, we observe stabilization and increased densification of cubic LLZO. This suggests the LiAlO$_2$ may be functioning as a sintering aid. The role of Li$_2$ZrO$_3$ is currently unclear, however, using an excess of Zr was essential to stabilize the cubic LLZO phase. LiAlO$_2$ accumulates at the surface forming a surface layer that helps to reduce the Li$^+$ loss during the calcination step, thereby preserving the structure integrity. This procedure interestingly yields phases that are lightly doped with Al^{3+} and slightly deficient in Zr. Our study indicates that the obtained LLZO phases contain ~0.12 mol Al per formula unit. This content is significantly lower than that used to stabilize the cubic garnet phase either by solid-state or sol–gel syntheses. Typically, $\geq$0.2 mol Al are used to make the Al-doped garnets at 1230 °C, and more Al is often observed in the materials due to reaction with the crucible.[6,9,11,14,15] The low content of the Al^{3+}-dopant in our material is clearly related to the synthetic strategy we employ, which avoids prolonged calcination at elevated temperature
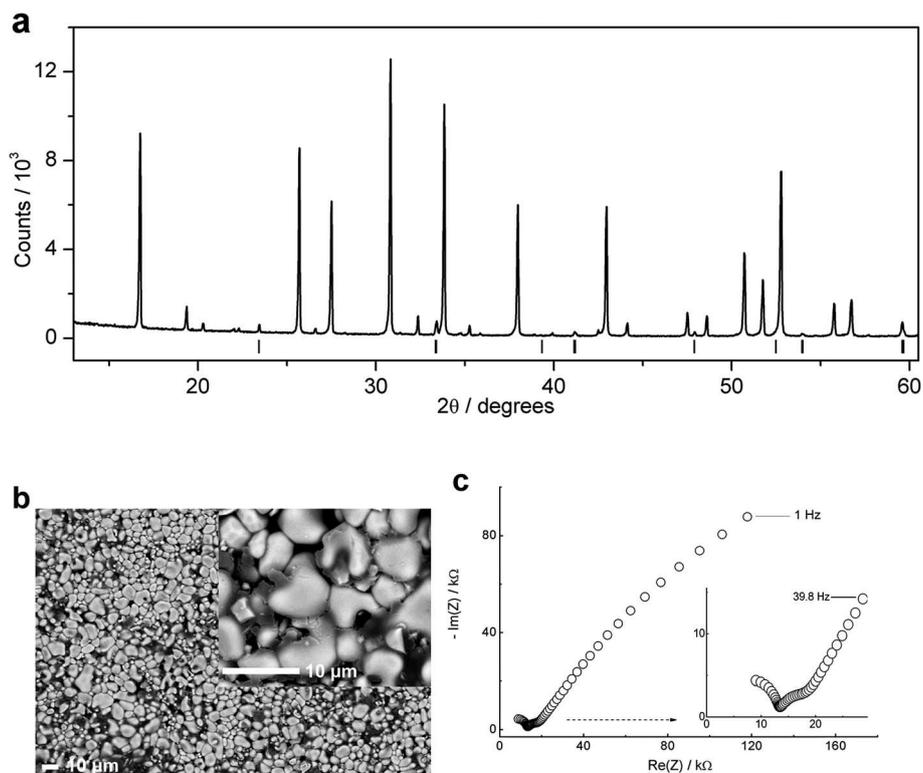
Fig. 10   (a) XRPD pattern for LLZO (2 wt% Al) synthesized by a conventional sol–gel procedure and calcined at 1100 °C; the markers are for LaAlO$_3$. (b) SEM image of the produced pellet. (c) A typical impedance plot for the material using gold electrodes at room temperature.

and also avoids intimate mixing of the LLZO and Al precursors (*e.g.* by ball milling).

It is widely accepted from theoretical and experimental points of view that the residence of Al in the 24d sites physically blocks the Li$^+$ pathways in the garnet lattice.[22,23] Hence, reducing the Al^{3+} content while preserving the cubic symmetry and sample sinterability is an advantage. Shin *et al.* provided theoretical and experimental evidence that reducing Al^{3+}-content in the 24d sites facilitates the lithium ion diffusion in the material.[22] This was reflected in the activation energy observed for the lithium ion transport in the material. A drop in the activation energy from 0.36 to 0.29 eV was observed when Al^{3+} is displaced from the 24d to the 96h sites due to Ta^{5+} incorporation (Li$_{7-3x-y}$Al$_x$La$_3$Zr$_{2-y}$Ta$_y$O$_{12}$). These findings are consistent with our results. The reduced Al^{3+} content in our material reduces the Al^{3+} occupying the lithium sites (including the 24d sites) to approximately one-half of the typical value, which is reflected in the activation energy observed for Li$^+$ conduction. The average activation energy observed in our materials is 0.28 eV, which is significantly lower than that observed for Al-rich phases previously reported.[1,6,11,16,17] In addition to the favoured Li$^+$ transport properties of the synthesized garnets, this developed synthetic procedure clearly realizes the formation of fast-ion conducting LLZO phases at relatively mild and highly controllable conditions. This procedure is suitable for large scale syntheses and is flexible in terms of using different starting materials and even different procedures to homogenize the parent LLZO solid precursor; the

developed synthesis of Al$_2$O$_3$ nanosheets is also simple and cost-effective. Our preliminary studies, in addition, suggest that this procedure is also an effective procedure to densify Li$_{7-x}$La$_3$Zr$_{2-x}$Ta$_x$O$_{12}$ phases which are important Li$^+$ solid electrolyte candidates and lack proper and reliable densification procedure.[31–33] Addition of 1 wt% Al (as Al$_2$O$_3$ nanosheets) to sol–gel processed Li$_{6.4}$La$_3$Zr$_{1.4}$Ta$_{0.6}$O$_{12}$ has significantly improved the sinterability and Li$^+$ conductivity of the material at relatively low calcination temperature (Fig. S10 and S11†). These studies are in progress in order to optimize phase purity, sinterability and ionic conductivity of different Li$_{7-x}$La$_3$Zr$_{2-x}$Ta$_x$O$_{12}$ phases.

4.   Conclusion

In summary, a simple hybrid sol–gel solid-state procedure has been developed to produce fast-ion conducting Al-doped LLZO phases *via* a single calcination step at 1100 °C for 3 h. This procedure greatly reduces the unreliability in accessing these garnets, which has been a matter of great concern in the solid state and energy materials communities. The cubic garnet phase is stabilized by incorporation of approximately 0.12 mol of Al per formula unit and the material is densified by the aid of LiAlO$_2$ formed *in situ* during the calcination step. LiAlO$_2$ forms a surface layer that helps to reduce lithium evaporation and preserves the structure during the high-temperature calcination. Excess Zr in the form of Li$_2$ZrO$_3$ is found to be essential to stabilize the cubic garnet phase. A slight Zr deficiency is also observed in these compounds. The materials show high total

and bulk conductivities and noticeable low ion-conduction activation energies. We attribute the ease of Li^+ diffusion in these materials to the low Al^{3+}-content that reduces hindrance to Li^+ three-dimensional movement in the lattice.

Acknowledgements

References

1 R. Murugan, V. Thangadurai and W. Weppner, *Angew. Chem., Int. Ed.*, 2007, **46**, 7778.

2 C. Ma, E. Rangasamy, C. Liang, J. Sakamoto, K. L. More and M. Chi, *Angew. Chem., Int. Ed.*, 2015, **54**, 129.

3 E. J. Cussen, *J. Mater. Chem.*, 2010, **20**, 5167.

4 H. Xie, J. A. Alonso, Y. Li, M. T. Fernández-Díaz and J. B. Goodenough, *Chem. Mater.*, 2011, **23**, 3587.

5 C. A. Geiger, E. Alekseev, B. Lazic, M. Fisch, T. Armbruster, R. Langner, M. Fechtelkord, N. Kim, T. Pettke and W. Weppner, *Inorg. Chem.*, 2011, **50**(3), 1089.

6 H. Buschmann, J. Doelle, S. Berendts, A. Kuhn, P. Bottke, M. Wilkening, P. Heitjans, A. Senyshyn, H. E. Ehrenberg, A. Lotnyk, V. Duppel, L. Kienle and J. Janek, *Phys. Chem. Chem. Phys.*, 2011, **13**, 19378.

7 E. Rangasamy, J. Wolfenstine and J. Sakamoto, *Solid State Ionics*, 2012, **206**, 28.

8 B. Xu, H. Duan, W. Xia, Y. Guo, H. Kang, H. Li and H. Liu, *J. Power Sources*, 2016, **302**, 291.

9 Y. Jin and P. J. McGinn, *J. Power Sources*, 2011, **196**, 8683.

10 H. Xie, Y. Li and J. B. Goodenough, *Mater. Res. Bull.*, 2012, **47**, 1229.

11 J. Sakamoto, E. Rangasamy, H. Kim, Y. Kim and J. Wolfenstine, *Nanotechnology*, 2013, **24**, 424005.

12 P. J. Kumar, K. Nishimura, M. Senna, A. Düvel, P. Heitjans, T. Kawaguchi, N. Sakamoto, N. Wakiya and H. Suzuki, *RSC Adv.*, 2016, **6**, 62656.

13 D. Rettenwander, G. Redhammer, F. Preishuber-Pflügl, L. Cheng, L. Miara, R. Wagner, A. Welzl, E. Suard,

14 N. Rosenkiewitz, J. Schuhmacher, M. Bockmeyer and J. Deubener, *J. Power Sources*, 2014, **278**, 104.

15 M. Amores, T. E. Ashton, P. J. Baker, E. J. Cussen and S. A. Corr, *J. Mater. Chem. A*, 2016, **4**, 1729.

16 L. Cheng, J. S. Park, H. Hou, V. Zorba, G. Chen, T. Richardson, J. Cabana, R. Russo and M. Doeff, *J. Mater. Chem. A*, 2014, **2**, 172.

17 K. Tadanaga, R. Takano, T. Ichinose, S. Mori, A. Hayashi and M. Tatsumisago, *Electrochem. Commun.*, 2013, **33**, 51.

18 A. Düvel, A. Kuhn, L. Robben, M. Wilkening and P. Heitjans, *J. Phys. Chem. C*, 2012, **116**, 15192.

19 A. A. Hubaud, D. J. Schroeder, B. Key, B. J. Ingram, F. Dogan and J. T. Vaughey, *J. Mater. Chem. A*, 2013, **1**, 8813.

20 D. Rettenwander, P. Blaha, R. Laskowski, K. Schwarz, P. Bottke, M. Wilkening, C. A. Geiger and G. Amthauer, *Chem. Mater.*, 2014, **26**, 2617.

21 D. Rettenwander, J. Langer, W. Schmidt, C. Arrer, K. J. Harris, V. Terskikh, G. R. Goward, M. Wilkening and G. Amthauer, *Chem. Mater.*, 2015, **27**, 3135.

22 D. O. Shin, K. Oh, K. M. Kim, K.-Y. Park, B. Lee, Y.-G. Lee and K. Kang, *Sci. Rep.*, 2015, **5**, 18053.

23 Y. Chen, E. Rangasamy, C. Liang and K. An, *Chem. Mater.*, 2015, **27**, 5491.

24 Y. Li, J.-T. Han, C.-A. Wang, S. C. Vogel, H. Xie, M. Xu and J. B. Goodenough, *J. Power Sources*, 2012, **209**, 278.

25 R. Wagner, G. J. Redhammer, D. Rettenwander, A. Senyshyn, W. Schmidt, M. Wilkening and G. Amthauer, *Chem. Mater.*, 2016, **28**, 1861.

26 A. C. Larson and R. B. Von Dreele, *General Structural Analysis System*, Los Alamos National Laboratory, Los Alamos, NM, 1994.

27 A. Dan'ko, M. Rom, N. Sidelnikova, S. Nizhankovsky, A. Budnikov and L. Grin, *Crystallogr. Rep.*, 2008, **53**, 1112.

28 H. El-Shinawi and J. Janek, *J. Power Sources*, 2013, **225**, 13.

29 J. T. S. Irvine, D. C. Sinclair and A. R. West, *Adv. Mater.*, 1990, **2**, 132.

30 W. B. Reid and A. R. West, *Solid State Ionics*, 1988, **28–30**, 681.

31 Y. Li, J. T. Han, C. A. Wang, H. Xie and J. B. Goodenough, *J. Mater. Chem.*, 2012, **22**, 15357.

32 H. Buschmann, S. Berendts, B. Mogwitz and J. Janek, *J. Power Sources*, 2012, **206**, 236.

33 K. Liu, J. T. Ma and C. A. Wang, *J. Power Sources*, 2014, **260**, 109.

M. M. Doeff, M. Wilkening, J. Fleig and G. Amthauer, *Chem. Mater.*, 2016, **28**, 2384.

This journal is © The Royal Society of Chemistry 2017

J. Mater. Chem. A, 2017, **5**, 319–329 | 329